- **Nanocatalysis: Size- and Shape-dependent Chemisorption and Catalytic Reactivity.** (B. Roldan Cuenya, et al, Surf. Sci. Reports 70, (2015) 135)

This review article focuses on correlating the catalytic reactivity of NPs and their geometry. It illustrated that chemisorption and catalytic properties such as the onset reaction temperature, the activity, and selectivity of a nanocatalyst may be tuned through controlled synthesis of NPs with well-defined sizes and shapes.

It has become clear that detailed information on the physical/chemical properties of supported NP systems must be available for the rational design of the next generation of nanosized catalysts. Such NP systems must be representative of active catalysts, and must be sufficiently well-defined (e.g., with respect to size and shape) to serve as a basis for theoretical modeling. In addition, a synergistic combination of in situ and in operando characterization techniques working under realistic reaction conditions (e.g. elevated temperatures and high pressure) must be available, since the working state of a NP catalyst might not be the state in which the catalyst was prepared, but a structural and/or chemical isomer that adapted to the particular reaction conditions. In order to address the complexity of real-world catalysts, a synergistic approach taking advantage of a variety of state-of-the-art experimental and theoretical methods must be undertaken. In this review, we have described some of the impressive developments that have been made in these areas. Many serious challenges still remain in the areas of catalyst characterization and design. One such challenge is to design highly active metal NP catalysts using abundant, inexpensive metals which can replace precious metal catalysts. Additionally, there is an increasingly pressing need for catalyst development for energy production applications, such as in fuel cells or for the synthesis of chemicals and fuels. Further work is needed to design more active and selective catalysts for these reactions that are viable at an industrial scale. In the coming years, nanocatalysis research must meet these challenges by building on the work described in this report. Further advancements in developing new synthetic methods will allow increased control over NP structure and stability, allowing for new insights into NP structure–reactivity correlations. In addition, the development of higher resolution in situ and in operando measurement techniques capable of probing catalytic reactions at NP surfaces over an extended range of temperatures and pressures and harsh environmental conditions will give unprecedented insight into NP catalysts in their working state. Single-nanoparticle spectroscopic and catalytic characterization must also be further developed. Advancements in computational modeling of more realistic catalysts will also bring us closer to gaining a molecularlevel view of a reaction at a NP surface when used to complement experimental studies. Such progress will bring us closer to realizing the goal of synthesizing highly effective, tailor-made, tunable nanoparticle catalysts.

- **Tuning Catalytic Selectivity at the Mesoscale via Interparticle Interactions.** (H. Mistry, et al, ACS Catal. 6, (2016) 1075)

Here, we present a comprehensive analysis on how the IP distance and size of NP ensembles affect their catalytic product selectivity for the electrocatalytic reduction of CO_2. Our analysis of reaction-diffusion processes at the mesoscale not only deconvolutes the individual roles of NP size and distance, but, more importantly, uncovers previously unaddressed principles governing the catalysis of NP ensembles in general, and that of the electroreduction of CO_2 in particular. We propose the "IP distance" as a largely overlooked, yet important experimental mesoscopic descriptor for selectivity that provides a deeper mechanistic understanding, as well as predictive control of catalyst activity and selectivity in the conversion of CO_2 to hydrocarbons.

The inverse micelle encapsulation technique allows for the synthesis of highly ordered NP arrays with a controlled, uniform size and tunable IP spacing. In this study, three different Cu NP sizes with various IP distances were synthesized using this method.

Figure 4.1 shows atomic force microscopy (AFM) images of 4.7 ± 1.2 nm NPs on a silicon support with a native oxide surface with the IP distance being varied from 53 nm to 24 nm. Cu NPs with average sizes of 1.5 ± 0.6 nm and 7.4 ± 1.8 nm were also prepared, with IP spacing ranging from 22 nm to 10 nm and from 92 nm to 41 nm, respectively. These IP distances were chosen in order to keep the ratio of IP distance to NP size (IP/d) in a similar range for each NP size, since this parameter can be used to compare diffusion phenomena on samples with different geometry.

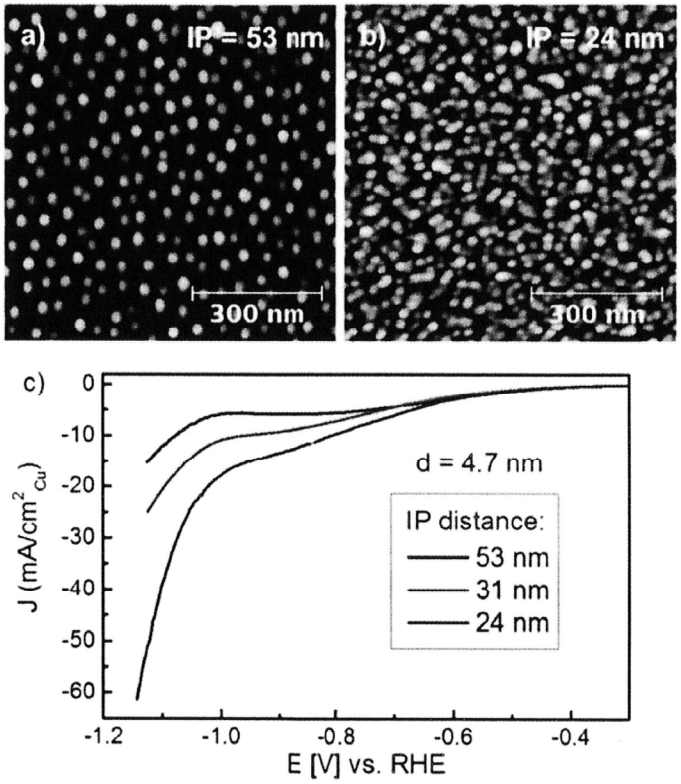

To characterize the catalytic activity of these NPs as a function of the IP distance, the NPs were deposited on glassy carbon plates and used as working electrodes during CO_2 electroreduction. Linear sweep voltammetry (LSV) voltammograms were measured up to a potential of E = −1.12 V vs RHE in 0.1 M $KHCO_3$. LSV measurements on the 4.7 nm NPs with various IP distances are shown in Figure 4.1c.

To investigate changes in selectivity with IP distance, reaction products were sampled using gas chromatography (GC) after 10 min of reaction at E = −1.12 V vs RHE, and Faradaic selectivity was calculated. The changes in Faradaic selectivity with IP distance for catalysts with three different sizes are shown in Figure 4.2. A change in Faradaic selectivity, as a function of IP distance, is observed for the 1.5 and 4.7 nm NPs

(Figures 4.2a and 4.2b), while a much smaller variation is detected for the largest (7.4 nm) NPs (Figure 4.2c). Interestingly, the 1.5 nm particles showed a different trend in selectivity from the 4.7 nm particles. To confirm the trend for the smallest NPs, the Faradaic selectivity for a similarly sized NP (1.9 nm) with an IP distance of 27 nm is also plotted in Figure 4.2a.

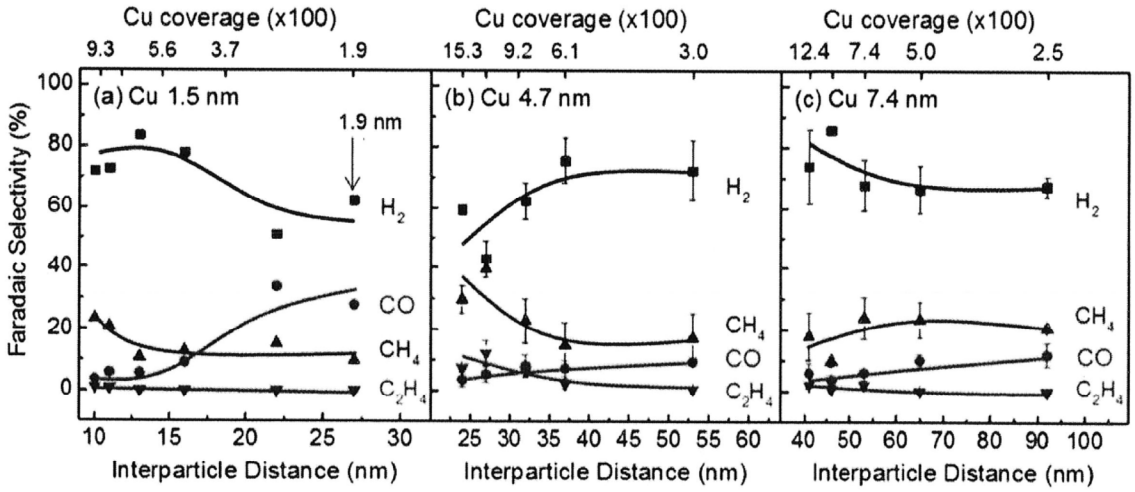

Figure. 4.2. Faradaic selectivity as a function of IP distance. Faradaic selectivity during the electroreduction of CO2 at E = −1.1 V vs RHE over (a) 1.5 nm, (b) 4.7 nm, and (c) 7.4 nm Cu NPs, as a function of the IP spacing. In panel (a), a data point for 1.9 nm NPs with an IP distance of 27 nm was added for reference. The top axis displays the copper coverage, defined as the ratio of the copper surface area to the surface area of the glassy carbon support. Lines are present to serve as guides for the eye. Error bars in panels (b) and (c) are calculated from two or more repeated measurements.

The complex trends observed in the Faradaic selectivities indicate that the activity and selectivity of NP catalysts for the CO_2 electroreduction reaction cannot be understood solely in terms of NP size and its effect on the binding strength of reactants. In addition to these nanoscale phenomena, mesoscale processes such as mass transport through diffusion, the readsorption of reaction intermediates on a given NP or, if spaced closely enough, on neighboring NPs should be considered.

The first mesoscale transport process that we will consider is the diffusion of reactants to the NP surface. Under our experimental conditions, the CO_2 bubbles fed into the reaction cell lead to a forced convection in the electrolyte and a uniform reactant concentration in the bulk of the electrolyte. However, very close to the electrode surface, the electrolyte may be considered stationary, and the diffusion process is the only pathway for mass transfer through this region. Mass-transfer transport phenomena within the diffusion layer determine how the reactants diffuse toward the NPs, as well as how the reaction products leave the NPs and enter the bulk of the electrolyte. Limitations in mass transfer are expected to hinder the reaction rate (e.g., current density).

In order to understand how mass-transfer effects may contribute to the electrocatalytic activity of our NPs, calculations were carried out to elucidate the changes in the CO_2 reaction rate, because of the diffusion processes. Finite element calculations were used to solve Poisson's equation and to obtain the spatial distribution of CO_2 at the NP surface. The diffusive flux of reactants, which is linearly proportional to the concentration gradient, was calculated following Fick's first law.

Figure 4.3a shows calculation results for 7.4 nm NPs with an IP distance of 36 nm. The surface of the upper hemisphere of the NPs provides a higher contribution to the reaction, since the electrolyte in contact with the bottom hemisphere of the NP has a lower concentration of the reactants (depleted red color region). Figure 4.3b shows the normalized CO_2 flux to the surface of NPs with different sizes (d = 1.5, 4.7, and 7.4 nm) and IP distance.

For a given NP size, Figure 4.3b shows that the normalized CO_2 flux is higher for NP arrangements with large IP distance and reaches a plateau for IP/d values larger than ~10. The latter represents a threshold value above which the NPs can be considered as single NPs on an infinite support. However, for smaller IP distances, NPs can affect neighboring particles by depleting their reactant concentrations. This phenomenon is observed as an overlap in the diffusion profile that limits the available reactant concentration on the NP surface and reduces the normalized CO_2 flux, which leads to a decrease in the current density of the CO_2 reduction reaction (Figure 4.3b). In Figure 4.3b, it is clear that the CO_2 flux saturates at a higher value for smaller NPs. However, the calculated reactant flux cannot be directly correlated to the current density, since the real number of electrons involved in the reaction per CO_2 molecule consumed is strongly dependent on the reaction products. Therefore, a large increase in the current density is expected when the selectivity shifts from CO and H_2 toward ethylene and methane. However, in cases where the selectivity remains almost constant, such as for our largest (7.4 nm) NPs, the electroreduction current will be proportional to the reactant flux. Figure 4.3c shows the experimental current density at −1.1 V vs RHE for the 7.4 nm NPs, as a function of the IP/d ratio, which shows good agreement with the trend in reactant flux obtained from theory in Figure 4.3b. The current density toward H_2 evolution will be similarly governed by the diffusion of H^+ to the NP surface. Figure 4.3b shows that above an IP/d ratio of ~10, the reactant flux to the NP surface reaches a plateau and is not strongly affected by further increasing the IP distance for each NP size. Therefore, it is reasonable to assume that, in the large IP distance regime, the NPs are sufficiently far away from each other that only the NP size influences the selectivity, not the IP distance.

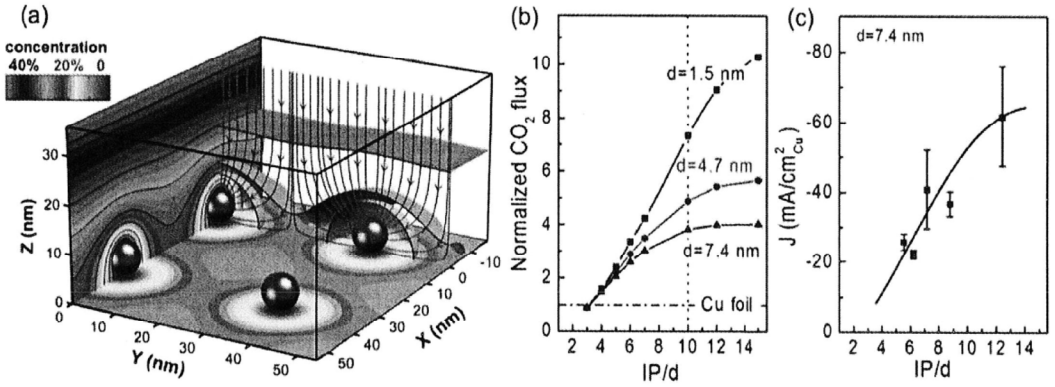

Figure 4.3. Calculations of CO_2 diffusion to the surface of NPs with different size and spacing, and corresponding experimental CO_2 electroreduction activity. (a) Simulation results of the CO_2 concentration distribution based on diffusion equations. The red arrows show the reactant flux toward the NPs. The color scale shows the concentration of CO_2 at a given distance from the NPs, as a percentage of its value in the bulk of the electrolyte. A diffusion layer thickness of 100 nm was assumed. (b) CO_2 flux obtained for NPs with different size and IP distances based on diffusion equations. The data are normalized by the corresponding flux obtained from a flat Cu foil. (c) Experimental current density obtained at −1.1 V (vs RHE) during the electrochemical reduction of CO_2 over 7.4 nm Cu NPs with distinct average IP spacing.

In order to see this size effect, the Faradaic selectivity was plotted as a function of NP size only for samples with the largest IP distances (see Figure 4.4). In addition to these three sizes, measurements of 1.9 and 2.3 nm NPs with large IP/d ratios (14 and 10, respectively) were added to confirm the trends for the smallest NPs. As expected, the readsorption and further reduction of reaction intermediates, such as CO, is limited by the decreased availability of neighboring particles, resulting in higher selectivity toward reaction intermediates for these samples. The H_2 and CO production do not vary for large NPs (4.7 and 7.4 nm), while there is a significant increase in CO and a suppression in H_2 production for the smallest NPs (Figure 4.4a).

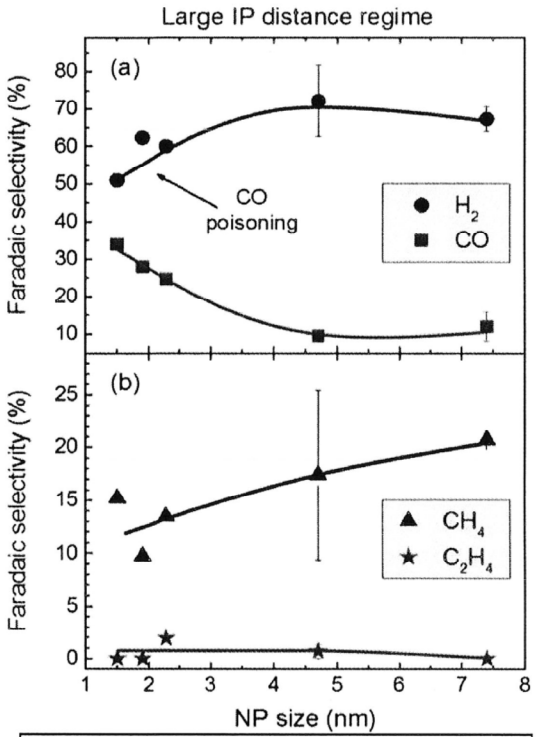

Figure 4.4. Faradaic selectivity in the large IP distance regime. Faradaic selectivity as a function of the NP size in the large IP distance regime (i.e., low Cu coverage), (a) for H_2 and CO and (b) for CH_4 and C_2H_4.

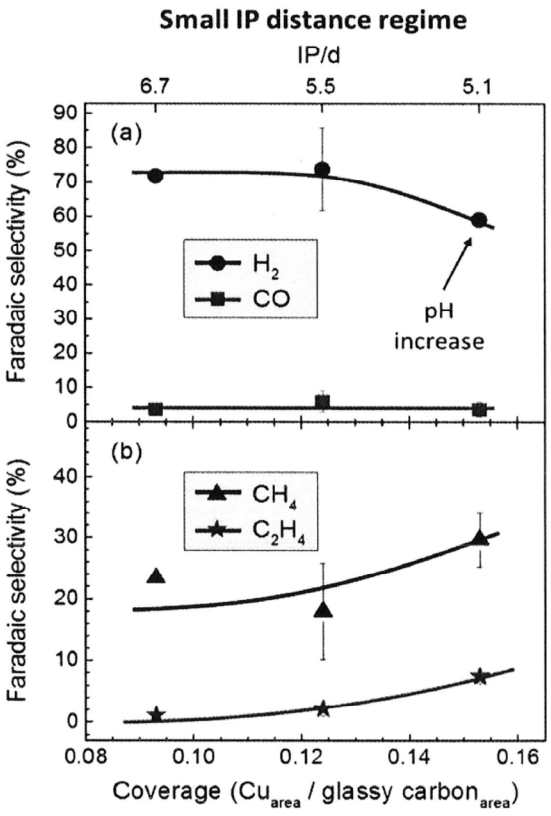

Figure 4.5. Faradaic selectivity in the small IP distance regime. Faradaic selectivity as a function of the copper coverage (bottom axis) and IP/d ratio (top axis) (a) for H_2 and CO and (b) for CH_4 and C_2H_4. Following our diffusion calculations, the Cu coverage was found to be the most representative parameter to describe the diffusion behavior of the reactant in a closely spaced NP system. Lines are present to serve as guides for the eye.

Because of the large IP distances considered here, the readsorption of reaction intermediate species originating from one NP onto a neighboring NP is unlikely. Therefore, self readsorption processes are likely the only pathways leading to hydrocarbon production. This explains why the C_2H_4 production pathway, where the largest number of reaction steps is involved, is low for all NP sizes (Figure 4b). Also, since the probability of intermediate self-readsorption is proportional to the NP size ($\propto d^2$), an increase in the CH_4 production rate is expected with increasing NP size, in excellent agreement with our experimental data.

For larger copper coverages, the IP distance may be small enough to allow the diffusive transfer of reaction intermediates between neighboring NPs. Therefore, in addition to the NP size, the IP distance should also be taken into account in order to understand the selectivity trends. The

Faradaic selectivity for the smallest IP distances of each NP size is shown in Figure 4.5, as a function of copper coverage and IP/d ratio, which are parameters that account for both NP size and IP distance. As discussed above, the readsorption of reaction intermediates on neighboring NPs will facilitate the multistep pathway required for hydrocarbon production, and this process should be significantly increased in the large copper coverage regime (e.g., small IP/d ratios). Figure 4.5 shows that there is a low CO selectivity and a high selectivity toward CH_4 and C_2H_4 with increasing coverage, in agreement with such readsorption phenomena. Very low CO production is expected due to the significantly higher hydrocarbon production, which consumes the CO intermediate.

We have demonstrated that exceptional control over the catalytic selectivity of Cu NPs of different size during the CO_2 electroreduction reaction can be achieved through variation of the IP distance. Through the synthesis and electrochemical characterization of Cu NPs with highly controlled size and spacing, we gained insight into mesoscale transport phenomena such as diffusion of reactants to the catalyst surface and readsorption of intermediate species. These results were further corroborated by theoretical calculations. Small IP distances are required to allow the readsorption and subsequent reduction of the CO intermediate to hydrocarbons. Larger NP sizes also allow the readsorption of reaction intermediates onto the same NP for further reaction, while small NPs may be affected by the poisoning of active sites by CO. This study highlights previously unaddressed aspects in our understanding of product selectivity through the exploration of mesoscale transport processes and mesoscopic descriptors, while building on current knowledge of nanoscale structure-reactivity correlations. But more generally, this work uncovers catalyst design principles of fundamental importance for many heterogeneously catalyzed chemical processes with multiple products occurring on the surface of NP ensembles. Such design principles can aid in improved chemical product selectivity and yields for energy and environmental needs.

- **Nanostructured electrocatalysts with tunable activity and selectivity.** (H. Mistry, et al Nature Rev Mat 1, (2016) 16009)

In this Review, we assess our current knowledge of tunable activity and selectivity in electrocatalytic processes that are controlled through the rational design of nanomaterials with well-defined structures. We focus on three key reactions for electrocatalytic energy production: the ORR, CO_2 electroreduction and the electrooxidation of ethanol. Heterogeneous metal and metal oxide catalysts were selected as model systems. For each reaction, the most promising catalysts are discussed, in addition to the structure-dependent mechanisms behind their enhanced performance. Such structural parameters include nanocatalyst size, shape, spacing, crystallographic orientation, chemical state, support material and composition (that is, the addition of a secondary or ternary metal). Finally, we discuss the remaining challenges and the outlook of future research directions.

We have demonstrated how rational control over the structure and composition of metallic nanocatalysts can be used to tune activity and selectivity for O_2 reduction, CO_2 reduction and ethanol oxidation, which are key reactions for emerging electrochemical energy conversion and storage processes. The main mechanisms behind the improved activity and selectivity in the nano-electrocatalysts discussed are summarized in FIG. 5.1.

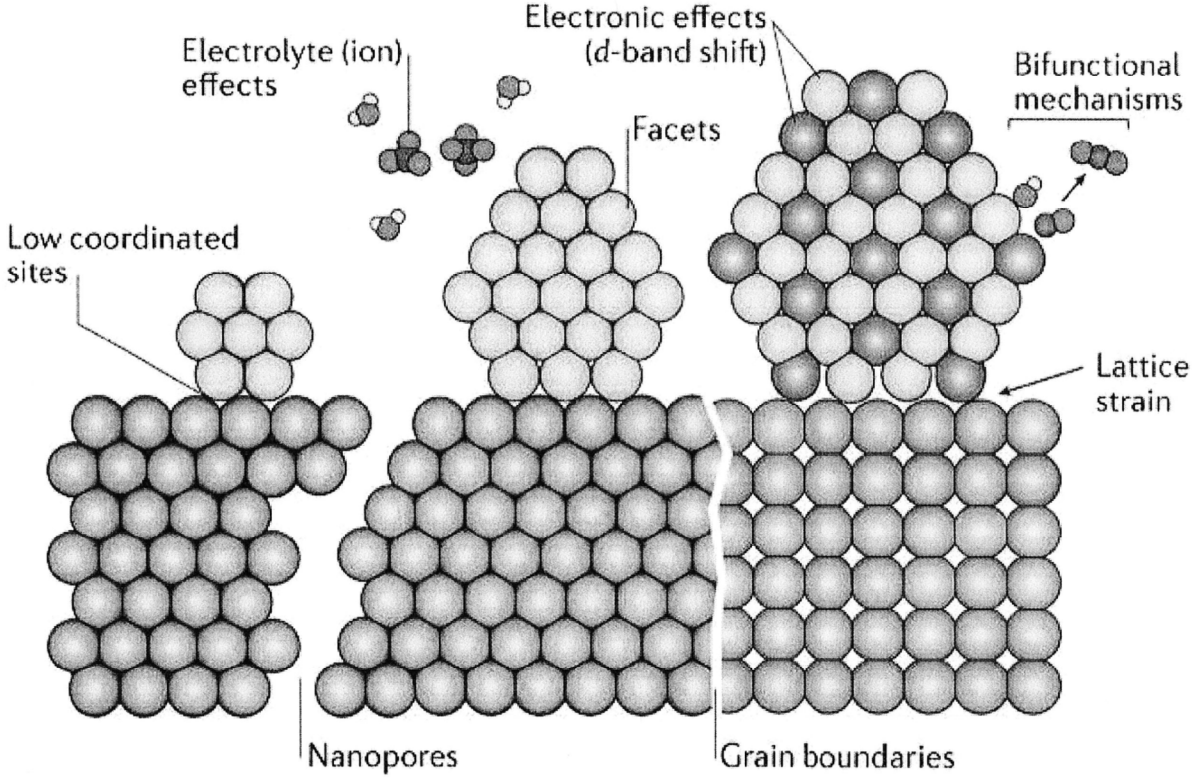

Figure 5.1. Overview of the mechanisms behind activity and selectivity control in nanostructured electrocatalysts. Structural features, such as low-coordinated sites, facets, nanopores and grain boundaries, can be tuned to control reactivity. In bimetallic nanostructures, strain effects, electronic effects and bifunctional effects can be tuned. In addition, reactivity trends may be strongly influenced by environmental factors such as the properties of the electrolyte and pH.

In terms of structure, morphology-controlled nanostructures may have the optimal particle size and/or shape to provide highly active, low-coordinated sites, such as corners and edges, or optimal facets that can facilitate a reaction step. Defects, such as grain boundaries, may also stabilize active sites. The interparticle distance is another crucial but often overlooked parameter that can be used to control the diffusion and readsorption of reaction intermediates and, therefore, the selectivity. Nanopores also provide low-coordinated sites for a reaction and can alter the selectivity by increasing the residence time of intermediates. For multimetallic catalysts, further mechanisms may contribute, such as geometric and ligand effects. Finally, in an electrochemical reaction, it is important to consider the effects of the electrolyte and ions in the solution, which may strongly adsorb on the catalyst surface, react with the surface to alter the structure or change the pH.

To develop feasible renewable energy technology based on fuel cells and to close the carbon cycle through CO_2 conversion, several key challenges in electrocatalyst design must be overcome. From the studies highlighted in this Review, it is clear that novel synthesis methods that allow for the design of model catalysts with control over the morphology, structure, chemical state and composition have enabled outstanding advances in the field of electrocatalysis. However, these synthesis methods must be scalable, and, particularly for the ORR and ethanol oxidation, new catalyst materials that are cheaper and more durable, or that can at least minimize the use of expensive Pt-group metals, must be developed. Another challenge is to better engineer selectivity for a single product to avoid separation costs, which is important for CO_2 conversion and for ethanol oxidation.

The nature of these catalysts is highly complex the nanostructure and active chemical species of the catalyst can be not only used to control the reaction but also changed during the reaction or by environmental factors such as the temperature and the properties of the electrolyte. Therefore, it is necessary to use *in situ* and *in operando* techniques to monitor the catalyst properties during the reaction to gain a complete understanding of the reaction mechanism. These techniques, combined with theoretical modelling, can provide an insight into the working structural and chemical states of the most active catalysts and provide the basic understanding needed to rationally design and tailor the properties of new catalysts.

- **Probing the Dynamic Structure and Chemical State of Au Nanocatalysts during the Electrochemical Oxidation of 2-Propanol.** (Y. Choi, et al, ACS Catal 6, (2016) 3396)

Gold NPs 1.0−11.0 nm in size prepared via reverse micelle encapsulation and deposited onto carbon foils were investigated for 2-propanol electro-oxidation in alkaline medium. NPs were characterized through atomic force microscopy (AFM), scanning electron microscopy (SEM), and X-ray photoelectron spectroscopy (XPS). Cyclic voltammetry (CV) was used to measure the catalytic behavior for 2-propanol oxidation. To understand morphological and chemical state changes in the NPs in their working state, operando X-ray absorption near-edge spectroscopy (XANES) and extended X-ray absorption fine structure spectroscopy (EXAFS) were employed. Our work highlights the dynamic nature of nanoscale catalysts and the importance of operando measurements for an understanding of structure− reactivity correlations and, in particular, of deactivation of nanocatalysts.

The NP morphology was characterized via AFM after deposition of the NPs on flat SiO_2/Si (100) substrates and ligand removal via O_2 plasma. Figure 6.1 shows AFM images of Au2 (1.1 nm) to Au5 (11.0 nm) NPs on SiO_2/Si (100). The real surface area of the Au NPs used for the normalization of our electrochemical data was calculated assuming spherical NPs. It should be noted that the NP diameters obtained via AFM on small NPs are not reliable due to tip convolution effects, and only the AFM NP heights can be used as representative size parameters.

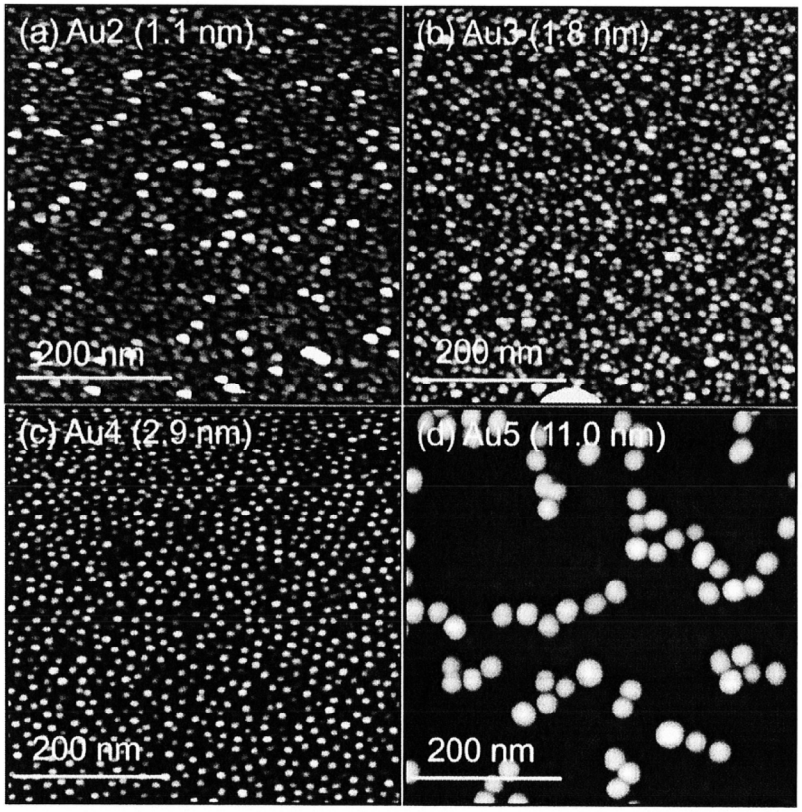

Figure 6.1. AFM images of Au NPs synthesized via reverse micelle encapsulation and supported on SiO2/Si(100): (a) Au2 (1.1 ± 0.7 nm); (b) Au3 (1.8 ± 0.5 nm); (c) Au4 (2.9 ± 0.6 nm); (d) Au5 (11.0 ± 1.5 nm).

SEM measurements were also acquired on the Au NPs supported on carbon foils in order to test the NP stability during the electrochemical reaction. Figure 6.2 displays SEM micrographs of the NPs in sample Au4 (2.9 nm AFM height) as prepared (Figure 6.2a,c) and after electrochemical 2-propanol oxidation (Figure 6.2b,d). An overall increase of the average NP size and partial agglomeration of the particles within favorable surface regions of the substrate are observed as a result of the electrochemical reaction.

Figure 6.3 shows the electrocatalytic performance of our Au NP/C samples during 2- propanol oxidation in an alkaline medium. The CV curves recorded between 0.73 and 1.34 V vs RHE were measured at room temperature in a mixture of 1.0 M 2-propanol and 1.0 M KOH at a scan rate of 5 mV/s.

In this work, the 2-propanol oxidation peaks of the reference Au foil were detected around 1.18 V, and the propanol oxidation peaks of the Au NPs were observed in a similar voltage range. Figure 6.3a shows that the electrochemical oxidation is remarkably influenced by the particle size, with the smaller NP catalysts having a lower onset potential for 2-propanol oxidation and higher current density.

The forward oxidation peak voltage ($E_{p,f}$) was shifted to a lower positive value with decreasing NP size, which also indicates the higher activity of the smaller NPs. Furthermore, the onset potential, defined here as the potential at which 1mA/cm^2 is reached, is also affected by the NP size (Figure 6.3b).

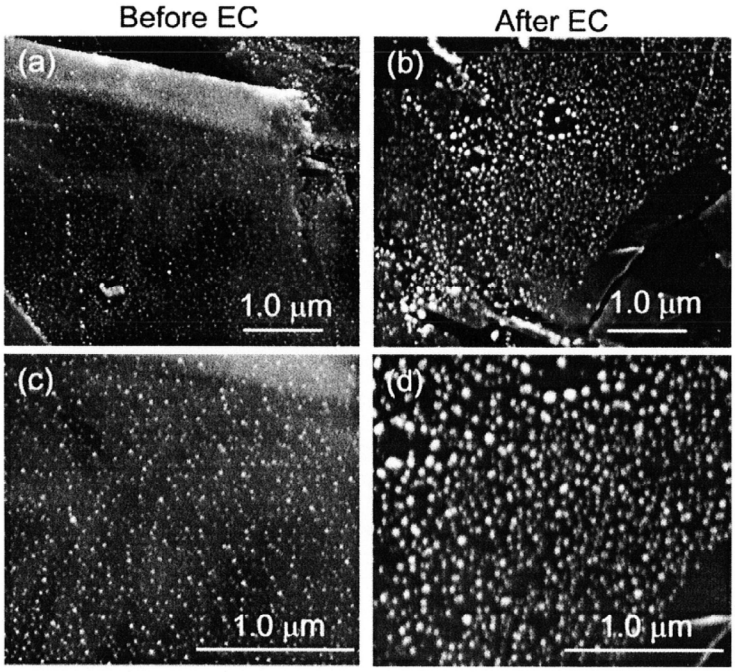

Figure 6.2. SEM images of Au4 (2.9 nm) NPs supported on a C foil acquired before (a, c) and after (b, d) electrochemical treatment.

It is possible for acetone to be formed from 2-propanol electrocatalytic oxidation as an intermediate, which could act as a catalyst poison. Unlike Pt catalysts, which can be severely deactivated by acetone produced during the anodic reaction, Au catalysts tend to be more tolerant to poisoning. The NP catalysts need to decompose the acetone adsorbed on the electrode surface to avoid deactivation. Table 6.1 contains the Jp,f/Jb ratio, known as catalyst tolerance, which is extracted from the oxidative peak current between the forward (Jp,f) and backward (Jb) CV scans. This ratio indicates the ability of the active sites of the NPs to resist acetone poisoning. Overall, the catalytic tolerance was found to increase with decreasing NP size, indicating that the anodic reaction (2-propanol oxidation) was increased for Au catalysts less than ~2 nm and that the acetone oxidation activity was also high. The differences observed in the $J_{p,f}/J_b$ ratio for the three samples containing NPs <2

sample	$J_{p,f}$(mA/cm$^2_{Au}$)	$E_{p,f}$ (V vs RHE)	2nd cycle	20th cycle
Au1 (1.0 nm)	17.88	1.128	3.89	2.23
Au2 (1.1 nm)	16.38	1.143	4.72	3.20
Au3 (1.8 nm)	13.64	1.162	4.77	3.57
Au4 (2.9 nm)	8.83	1.167	3.55	3.37
Au5 (11.0 nm)	4.23	1.190	2.93	2.24
Au foil	2.77	1.168	1.84	2.28

nm might be related to the distinct NP size distributions and the interplay between the enhanced activity for 2-propanol and acetone oxidation. In addition, a comparison of the $J_{p,f}/J_b$ ratio for all samples between the 2nd cycle and 20th cycle shows a deterioration of the catalyst tolerance, meaning that the catalyst lifetime is decreased in the course of the electrochemical reaction. The same phenomenon is shown in Figure 6.4, which displays the peak current for 2-propanol oxidation as a function of time. The decrease in activity with time could be due not only to the poisoning effect described above but also to any possible changes in the NP structure under reaction conditions. For example, an increase in the NP size would modify the chemisorption properties of the NPs, which would also lead to catalyst deactivation given the size–reactivity correlation shown above. Changes in the morphology of the active catalysts under operando conditions will be described in the next section on the basis of the analysis of XAFS data. Such changes might be more drastic for the smaller NPs (which are more dynamic in size and shape and more easily modified under reaction conditions), which could explain the drastic change in the Jp,f/Jb ratio for NPs smaller than 2 nm, as for example the ~1 nm NPs in sample Au1, which are likely to undergo significant restructuring under reaction conditions. The comparison with a bulk Au foil in Figure 6.4 reveals that, after an initial activation period, the gold foil reaches a stable activity, while for all NP samples, although the initial activity was higher than that of the foil, deactivation is observed over time.

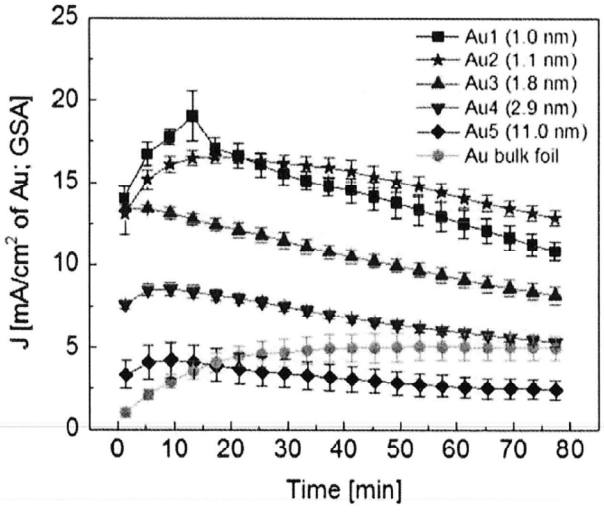

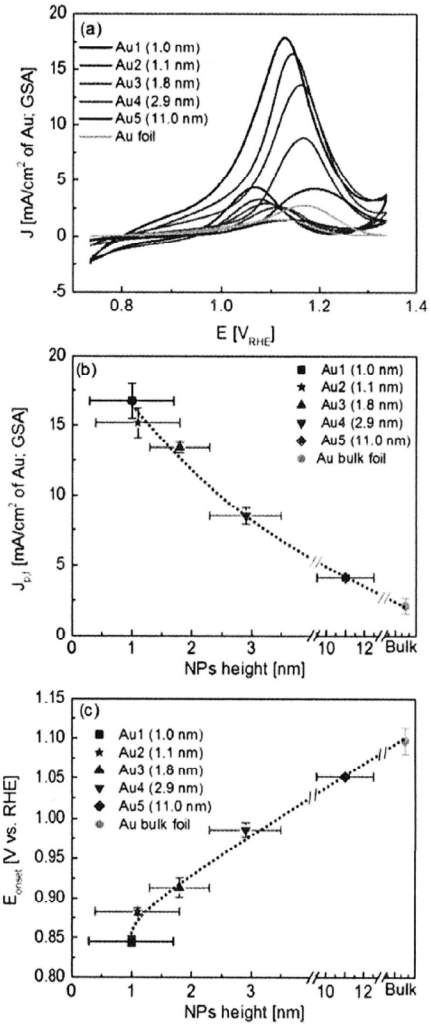

Figure 6.3. (a) CV curves of 2-propanol electrochemical oxidation over Au NP/C catalysts obtained at room temperature with a sweep rate of 5 mV/s in 1 M 2-propanol with 1 M KOH. (b) Maximum peak current density of 2-propanol oxidation during the forward scan vs nanoparticle height. (c) Onset potential for 2-propanol oxidation at 1 mA/cm2 vs NP height. The dashed lines are guides for the eye.

Figure 6. 4. Temporal evolution of the current density of the 2-propanol oxidation peak (anodic CV scan, Jp,f) obtained for all Au NP/C samples and a reference bulk Au foil. The error bars correspond to the average of three measurements conducted on identically synthesized but separate fresh samples of the same type (same average size).

Figure 6.5 shows Tafel plots derived from the logarithm of the current density in Figure 6.3a. Shown in Table 6.2 are the values of the Tafel slopes within the lower anodic polarization curve region (0−50 mV), the higher anodic polarization curve region (100−300 mV), and the exchange current density (io), which relates the rate of charge transfer when forward and reverse 2- propanol oxidation are in equilibrium. The smaller NPs, Au1 (1.0 nm)−Au4 (2.9 nm), have a lower Tafel slope and higher exchange current density than the largest NPs in sample Au5 (11.0 nm), implying that they are more efficient catalysts for 2- propanol oxidation. Surprisingly, the largest NPs have a higher Tafel slope in comparison to bulk Au. It was also observed in Figure 6. 4 that, over time, the catalytic performance of Au5 (11.0 nm) became worse than that of the gold foil. These data may indicate that Au5 (11.0 nm) has a higher population of unfavorable sites or facets for 2-propanol oxidation, which are more easily poisoned during the reaction.

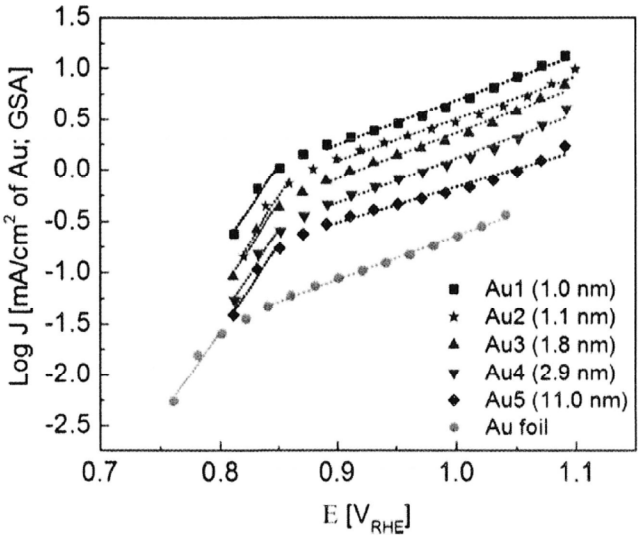

Figure 6.5. Tafel plots of 2-propanol electro-oxidation over Au NPs/C in 1 M 2-propanol with 1 M KOH. Linear Tafel slope fits (dotted lines) in two different anodic polarization regions are also shown.

Figure 6.6 displays XAFS data of Au4 (Figure 6.6a,b) and Au3 (Figure 6.6c) samples measured in different states, including under operando conditions during 2-propanol electrooxidation. The inset in Figure 6.6a shows the so-called white line of the XANES spectra of the catalyst measured before, during, and after the reaction.

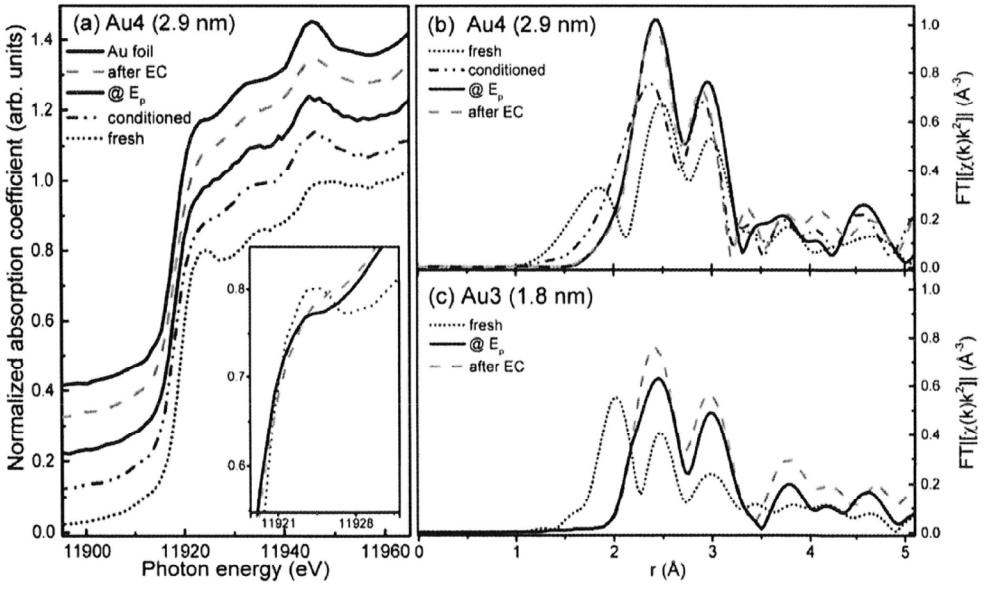

Figure 6.6. Au L3 edge XAFS spectra. (a) Near-edge structure (XANES) of sample Au4 (2.9 nm) as prepared (red), after electrochemical conditioning in the electrolyte by 20 CVs (green), under operando conditions during 2-propanol electrooxidation (blue), and after all electrochemical testing (orange) in comparison with a gold foil reference spectrum (black). The inset gives a comparison of the white-line intensities. (b, c) display k2- weighted EXAFS spectra of samples Au4 (2.9 nm) and Au3 (1.8 nm), respectively (Fourier transform k range 2.5−11.1 Å−1). The operando measurements were performed at the forward peak voltage values (Ep,f) given in Table 6.1.

The spectra of the fresh samples have a small peak at ca. 11924 eV (white line) indicating mild gold oxidation arising from the O2 plasma ligand removal procedure used in the NP synthesis. This peak is not observed in sample Au4 (2.9 nm) after voltage cycling, apparently due to the removal of oxidized species from the metallic NP surface during CV conditioning. XANES spectra of all samples taken after the reaction resemble those of a metallic Au foil in terms of their reduced chemical state. EXAFS spectra of the Au4 (2.9 nm) and Au3 (1.8 nm) samples in r space are depicted in Figure 6 b,c, respectively. The fresh samples show a peak at 1.9 Å (uncorrected for phase shift), which can be attributed to a light backscatterer in the local Au environment. Residuals of Cl from the gold precursor salt or N from incompletely removed polymer ligands covering the Au NP surface are good candidates for such a light atom in the first coordination shell of gold. However, these were not detected with XPS. The low r peaks also do not fit with a FEFF model of a bulk-like Au2O3 structure. Most likely, those peaks represent weakly bound chemisorbed oxygen covering the gold NPs or a disordered surface gold oxide, which do not give rise to an ordered bulk-like gold oxide structure. Metallic Au−Au backscattering is represented on all spectra with two peaks at 2.4 and 3.1 Å (phase uncorrected) and indicates the presence of a metallic core in the fresh samples. The metallic EXAFS features show significantly lower amplitude (i.e., lower coordination numbers) in comparison to bulk Au (not shown) due to the small NP size. However, the magnitude of the EXAFS Fourier transformed features increases for the samples under operando conditions and after the electrochemical experiments. Thus, according to the results of EXAFS fitting, the fresh Au3 sample (1.8 nm average AFM height) has a metallic Au−Au coordination number (CN) of 6.6, which then increases to 8.8 under operando conditions and finally reaches 9.8, which corresponds to ~2.3 nm using a spherical particle model. Similarly, sample Au4 (2.9 nm) has a Au−Au CN of 8.9 in the fresh state, which increases to 11.0 after CV conditioning and 11.5 under operando conditions and reaches 12.0 after all electrochemical tests. Since a coordination number of 12 corresponds to a bulk gold metal fcc structure, our results indicate significant particle size growth.

Summarizing, our XAFS data reveal that the initially cationic gold species present in our samples are decomposed under reaction conditions and that the NPs increase in size during the reaction, which likely correlates with the decrease in activity that we observe with increasing reaction time (or number of reaction cycles).

In summary, our experimental results revealed that the catalytic activity of the Au NPs for 2-propanol oxidation was strongly influenced by the NP size. XAFS and XPS data showed that cationic Au species present in the as-prepared samples are not stable under reaction conditions and are reduced during the electrochemical cycle, with metallic Au being the active species for the reaction. The increased activity of the smaller NPs for the total oxidation of 2-propanol to CO_2 may be explained by the higher population of low-coordinated sites with distinct adsorbate binding properties. The latter likely leads to enhanced activity for the oxidation of poisoning intermediates such as acetone. In addition, evidence for an increase in Au NP size is observed under catalytic reaction conditions, which can at

least in part explain the temporal evolution of the catalyst performance, in particular the progressive deactivation observed for the nanosized catalysts.

- **Highly selective plasma-activated copper catalysts for carbon dioxide reduction to ethylene.** (H. Mistry, et al, Nature Comm. 7, (2016) 12123)

We have used oxygen (O_2) and hydrogen (H_2) plasmas to create novel nanostructured oxide layers and porous surfaces with tunable morphology and chemical state on polycrystalline Cu for electrocatalytic reduction of CO_2. These catalysts can lower the onset potential of CO_2 reduction to ethylene by 350 mV compared with electropolished Cu, with a maximum faradaic selectivity of >60% at −0.9 V versus RHE. Here, using a combination of characterization techniques—including operando X-ray absorption fine-structure spectroscopy (XAFS), scanning transmission electron microscopy (STEM) equipped with energy dispersive X-ray spectroscopy (EDS)—we gain insight into the catalysts in their working state and find that Cu^+ is the active species for reducing CO_2 to ethylene. Through our results, we unravel the mechanism behind the improved activity and unique ethylene selectivity of oxide-derived Cu catalysts and lay out the design principles necessary for improved ethylene-selective CO_2RR catalysts.

To synthesize plasma-activated Cu, electropolished polycrystalline Cu foils were treated in O_2 and H_2 plasmas of varying power and duration. Figure 7.1 presents scanning electron microscopy (SEM) images of the Cu films treated with O_2 plasma at 20 W for 2 min (top row) and 100 W for 2 min (middle row) and 10 min (bottom row). By tuning the plasma conditions, the morphology of the surface and oxide thickness can be easily controlled. Growth of the Cu oxide begins at grain boundaries, forming micron-sized wires as shown in Fig. 7.1a. With increasing plasma time and power, the wires merged, forming a highly roughened surface, (c.f. Fig. 7.1b,e,i) and became highly porous with an observed 64% increase in the number of pores and 50% decrease in pore size. Subsequently, the plasma-activated Cu samples were partially reduced *in situ* during CO_2RR, and the resulting surface morphology is shown in the last column of Fig. 7.1. For most samples, an increase in the porosity was observed. Interestingly, the sample oxidized at 100 W for 10 min showed the growth of hair-like nanoneedles after the reaction. To compare the effect of plasma reduction on the film morphology to the electrochemical reduction mentioned

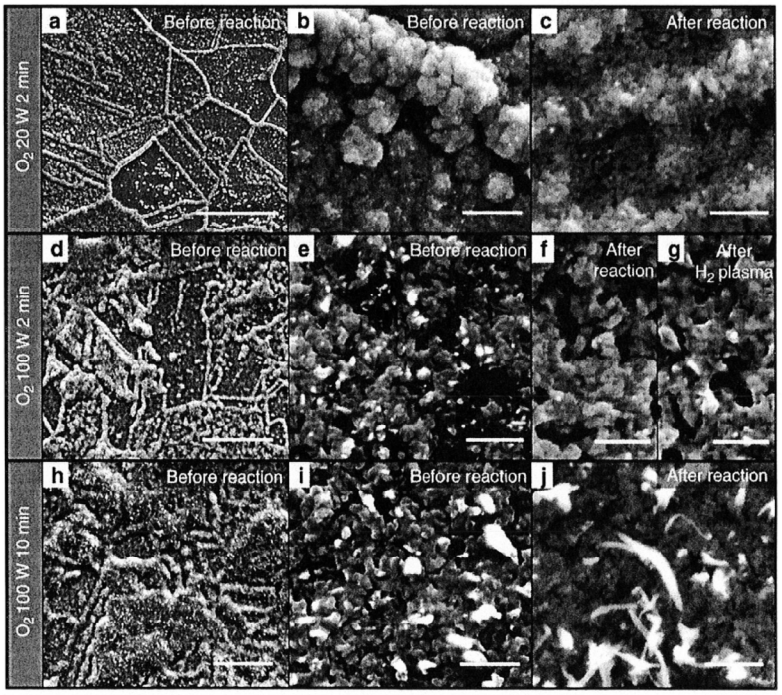

Figure 7.1. Morphological characterization of plasma-treated Cu foil electrodes. SEM images of Cu foils treated with O2 plasma for (a–c) 20W 2min; (d–g) 100W2 min; and (h–j) 100W10 min. (a,b,d,e,h,i) The morphology of the as-prepared foils. (c,f,j) The morphology after the CO2RR reaction. (g) The sample plasma treated with O2 at 100Wfor 2 min after an additional H_2 plasma treatment at 100Wfor 10 min. Scale bars, (a) 10mm; (b,c,e–g,i,j) 500 nm; (d,h) 20mm.

above, a H_2 plasma was used (100 W for 10 min), and is shown in Fig. 7.1g. The resulting structure was very similar to the electrochemically reduced sample (c.f. Fig. 7.1f), indicating that plasma reduction or electrochemical reduction of the Cu oxides results in a similar structure.

To gain further information on the structure and chemical state of the plasma-treated Cu films, cross-sections of the samples were measured using STEM combined with elemental mapping using EDS. Cross-sectional EDS maps of plasma-treated Cu samples before and after CO_2RR are shown in Fig. 7.2. After the O_2 plasma treatment, the EDS maps show two well-defined oxide layers over the bulk metallic Cu film. Stoichiometric analysis using EDS data resulted in Cu:O ratios of 2.7:1.0 and 1.3:1.0 for the interlayer and upper layers, respectively, indicating that the interlayer is Cu_2O, while the upper layer is copper(II) oxide (CuO). It is also apparent that at grain boundaries and crystallographic domains with the fastest oxide growth, a thick 1.5-μm Cu_2O interlayer grows with a thinner 100 nm CuO top layer, while in domains with slower oxide growth, the CuO layer is thicker at 260 nm—as clearly shown in Fig. 7.2a. Figure 7.2g shows the 100 W 2 min oxidized Cu with a subsequent H_2 plasma treatment. A 100 nm layer at the surface is reduced entirely to metallic Cu, with the CuO and Cu_2O oxide layers being still observed subsurface. After H_2 plasma treatment, the sample was exposed to air for more than a week before TEM sample preparation and analysis, and the native Cu oxide layer, measured to be <3 nm thick, was insignificant compared with the thick oxide layers which formed from the plasma treatment and remained during the reaction. This indicates that the observed oxides in our samples before or after reaction are not simply due to surface oxidation in air during the *ex situ* sample transfer to the TEM. Figure 2c,f,h also shows EDS maps of these samples after 1 h of CO_2RR at −0.91 V versus RHE. Remarkably, after the reaction a single layer with O atom concentration ranging from 3 to 29 atomic % remains with porous and oxygen-rich regions observed. The Cu oxide species are present throughout the layer, indicating that the surface is rich in Cu^+ sites which remain stable on the surface and near surface layers during the reaction. This finding challenges the conventional assumption that only metallic Cu (Cu^0) is the active species during CO_2RR and indicates that Cu^+ plays a significant role in the unique reactivity of oxide-derived Cu.

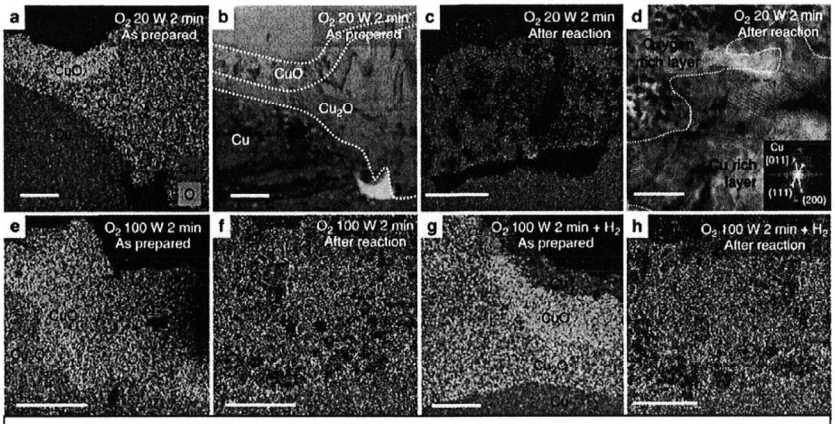

Figure 7.2. EDS elemental maps of Cu foils treated with O_2 plasma for (**a–d**) 20 W 2 min; (**e–f**) 100 W 2 min; and (**g–h**) 100 W 2 min+H_2plasma. The images labelled 'after reaction' were used as catalyst for CO_2RR for 1 h at −0.91 V versus RHE. (**b,d**) HRTEM and SAED analysis of the O_2 plasma 20 W 2 min treated sample before and after the reaction, respectively. Scale bars, (**a–c**) 300 nm; (**d**) 20 nm; (**e–h**) 200 nm.

Figure 7.2b,d show high-resolution TEM (HRTEM) and selected area electron diffraction (SAED) patterns of the O_2 20 W 2 min plasma-treated sample before and after the reaction. The diffraction analysis confirms that a CuO top layer and Cu_2O interlayer exist before the reaction (Fig. 7.2b). After the reaction, the layer transforms

into a mixture of Cu-rich regions, which contain only 3.4±0.9% oxygen atoms, and oxygen-rich regions with 19.5±2.6% oxygen atoms identified as Cu_2O. It is clear that the oxygen is depleted during the reaction, but the surface layer of the oxidized Cu films is still rich in oxygen even after 1 h of reaction. It is unlikely that the Cu oxides in the sample after reaction could be a result of air exposure, since the native oxide would be much thinner due to its slow growth rate at room temperature in air and would contain Cu(II) species, which are not observed here.

To further investigate the changes in the structure of the oxide layer during CO_2RR and gain insight into the chemical state of the active Cu species, operando X-ray absorption near-edge structure (XANES) and extended XAFS (EXAFS) were used. Figure 7.3 shows the Cu K-edge XANES and EXAFS spectra of the O_2 100 W 2 min plasma-treated Cu measured in fluorescence at small incidence angle (for enhanced surface sensitivity) during CO_2RR at −1.2 V versus RHE. Although the thickness of the sample caused dampening of the XAFS signals due to self-absorption, the XANES spectrum of the as-prepared plasma-oxidized Cu shows the features of Cu_2O, in particular, the prominent shoulder at the edge marked with a green dashed line at ~8,982 eV. The presence of metallic Cu and Cu oxide in the initial sample is also clear in the EXAFS data shown in Fig. 7.3b,c. During the first 15 min of reaction, a combination of Cu and Cu_2O features are still present, and at 1 h, only metallic Cu features are discernable. Although an oxygen content of ~25–28% is still present in the surface layer of the catalyst after 1 h of reaction according to STEM-EDS, XAFS probes further into the bulk, and when the films are partially reduced, the XAFS signals become dominated by the signal of the metallic Cu underlayer. Nevertheless, we have shown here unquestionably that for our plasma-oxidized Cu catalyst, Cu_2O species are present and can participate in the reaction. It is clear that significant changes occur in the bulk of the Cu oxide layer during the first 15 min of reaction in which the initial CuO and Cu_2O layers are reconstructed and some of the oxygen is depleted. After this initial change, it is likely that the Cu_2O species remain relatively stable in the surface layer, since the activity and selectivity measured after 10 min and 1 h are unchanged for all the oxidized samples. Furthermore, the reactivity of the O_2 20 W 2 min sample was observed to be stable over the course of 5 h, suggesting there is no significant change on the

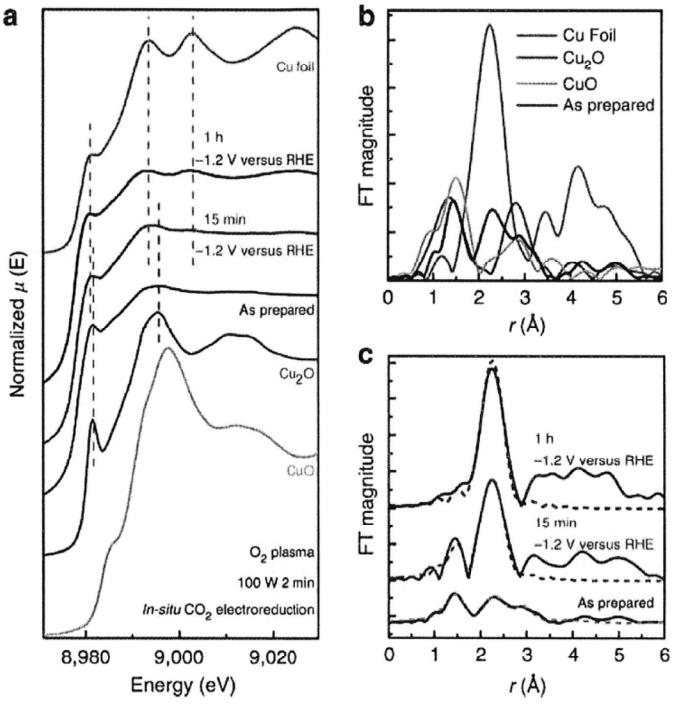

Figure 7.3.(**a**) XANES spectra of the O_2 100 W 2 min treated sample measured under operando conditions in 0.1 M $KHCO_3$ during the first 15 min and after 1 h of reaction at −1.2 V versus RHE. Bulk Cu, Cu_2O and CuO spectra are plotted as reference. (**b**) EXAFS spectrum of the as-prepared sample plotted with references. (**c**) EXAFS spectra and fits (dashed lines) of the sample measured under operando conditions. Fourier transforms are k^2-weighted.

active phase during this time. Therefore, it is likely that Cu^+ species can be supplied to the surface from the thick initial oxide surface and subsurface layers during the reaction to maintain the reactivity of these catalysts over time.

The catalytic activity and selectivity of the plasma-activated copper foils were studied by performing bulk electrolysis in 0.1 M potassium bicarbonate ($KHCO_3$) at a constant potential and analysing the reaction products via chromatographic techniques. Figure 7.4 shows the geometric current density as a function of applied potential. The plasma treatment has a clear effect on the activity of Cu towards CO_2RR which can partially be attributed to the surface roughness. In general, longer and higher power O_2 plasma treatment increases the roughness factor, which is an estimate of the active surface area derived by measuring the double layer capacity and normalizing by the electropolished foil. However, roughness effects alone cannot explain all of our experimental findings satisfactorily. In fact, the initial oxidation state of the sample also affects the current density. This is particularly evident when we compare the catalytic activity of the O_2 100 W 2 min and O_2 100 W 2 min+H_2 plasma-treated Cu. Although both samples have a similar surface roughness, their catalytic activity is significantly different. The H_2 plasma treatment on the oxidized sample reduces the activity by about two times compared with the oxidized sample without H_2 treatment. The H_2 plasma treatment depletes the oxide species available initially in the sample, as shown in Fig. 7.2g, while having minimal effect on the surface roughness. This result is an indication that the Cu oxide species are critical for improved current density. As demonstrated by our STEM-EDS data, even after 1 h of CO_2RR, patches of Cu_2O are still observed near the sample surface.

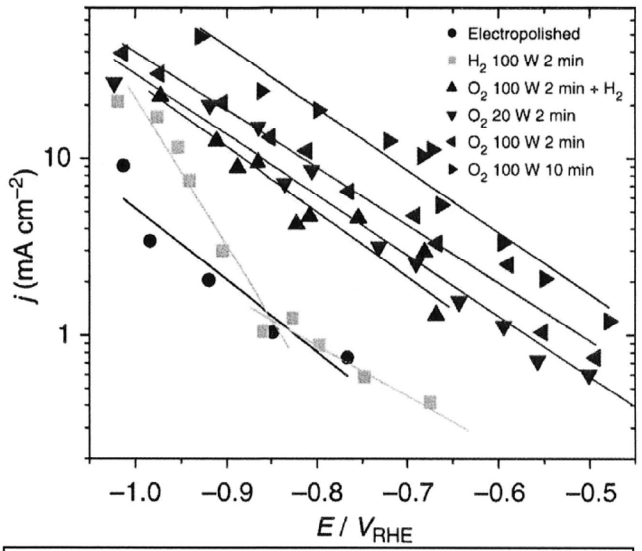

Figure 7.4. Geometric reduction current density as a function of applied potential.

Figure 7.5 shows the faradaic selectivity of the CO_2RR products for the plasma-activated Cu samples as a function of applied potential. The plasma treatments not only affect the activity of copper, but more importantly, they also have a remarkable effect on selectivity. The selectivity change is most drastic on the O_2 treated samples: on one hand, this treatment clearly suppresses methane formation (Fig. 7.5c), while on the other hand, it enhances the formation of the other products of CO_2RR (CO, formate and ethylene). We observe that the onset potential towards CO and formate ($HCOO^-$) is shifted to lower overpotentials. Furthermore, for our plasma-oxidized Cu, the selectivity towards CO reaches a maximum of 60% at −0.5 V versus RHE, which is three times higher than for electropolished Cu foil. In our study, the onset of ethylene production is also shifted from approximately −0.85 V versus RHE for metallic Cu foils to as low as −0.5 V versus RHE for the most oxidized

Cu foils. In addition, we observe a remarkably high selectivity towards ethylene, reaching 60% at −0.9 V versus RHE for the O_2 20 W 2 min plasma-treated sample. This value is higher than other oxide-derived Cu catalysts synthesized from thermal oxidation, which show <10% ethylene efficiency at these potentials, or from electrodepositon of Cu_2O. In addition, the most oxidized foils in this study also produce trace amounts of ethanol. Interestingly, the 100 W O_2 plasma-treated samples, which have been exposed to a stronger oxygen plasma treatment and are characterized by the highest roughness factors, also produce trace amounts of ethane, but nonetheless exhibit lower C_2H_4 selectivities. These results indicate that there is an optimal oxidation treatment to favor ethylene formation. We hypothesize that this trend could be related to mass diffusion limiting ethylene formation on the most roughened surfaces where high geometric currents are achieved. This is also consistent with our observation that at high overpotentials at which high geometric current densities are also achieved ethylene selectivity is suppressed.

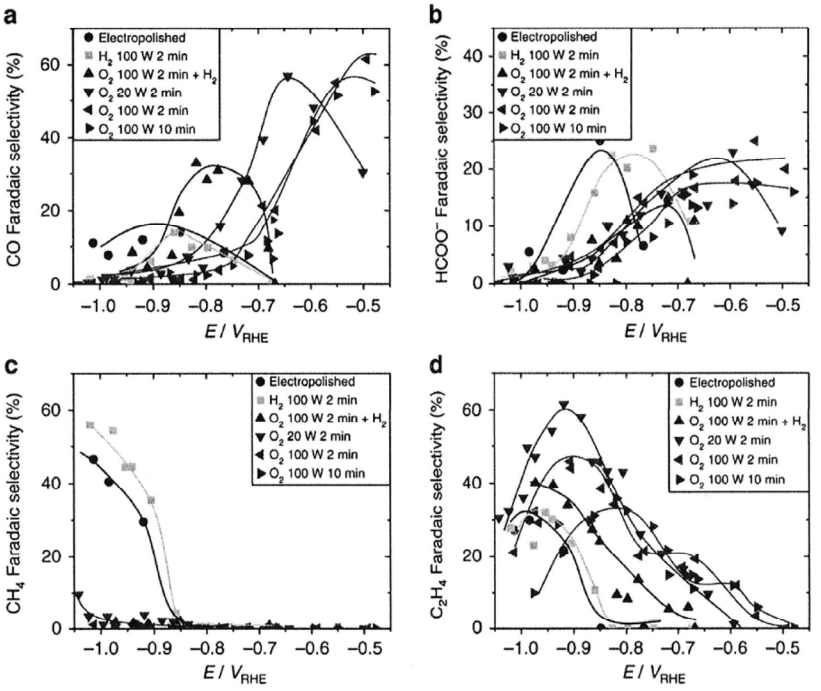

Figure 7.5. Data were acquired after 60 min of CO_2 electrolysis at a constant potential in CO_2 saturated 0.1 M $KHCO_3$. (**a**) CO, (**b**) formate, (**c**) CH_4 (**d**) C_2H_4. Solid lines are guides for the eye.

By comparing the catalytic performance of O_2 plasma 100 W 2 min+$H_2$and O_2 plasma 100 W 2 min Cu, we have demonstrated that purely a roughness effect cannot explain the reactivity trends of our plasma-activated oxide-derived Cu catalysts, since these catalysts with nearly the same roughness, but different oxide content have significantly different reactivity and selectivity. Based on our STEM-EDS and operando XAFS measurement we conclude that, contrary to common belief, Cu^+ species are stable under reaction conditions and play a determining role in the reactivity of oxide-derived Cu. These species may interact with negatively charged CO_2 reduction intermediates which may play an important role in determining selectivity.

The mechanism behind the stability of Cu^+ species under the thermodynamically unfavourable conditions of CO_2RR is still under investigation, however, several mechanisms may explain this phenomenon. One possibility is that the highly roughened surfaces with low-coordinated sites which are formed after O_2 plasma treatment may bind more strongly to oxygen, helping to stabilize oxides during the reaction. Strain in the surface caused

by the oxidation and reduction of the surface may also cause strong oxygen binding. The highly porous nature of the films formed might also serve as favorable oxygen reservoir. Another possibility is that the high local pH could help to stabilize Cu^+ by negatively shifting the overpotential for Cu_2O reduction. While similar stability of Cu^+ has been suggested for oxide-derived Cu catalysts, we provide here the first direct evidence that Cu^+ species are stable during CO_2RR and are key for controlling selectivity.

In summary, we have synthesized superior oxygen-derived Cu catalysts using plasma treatments and used a synergistic combination of advanced *ex situ*, *in situ* and operando techniques to reveal the key mechanisms behind the improved performance of oxide-derived copper catalysts. Plasma treatment was found to be a facile method to rapidly oxidize Cu foils, which resulted in stable oxide layers with a unique surface structure. These plasma-oxidized catalysts achieve lower onset potentials for CO, formate and ethylene, as well as outstanding ethylene selectivity of 60% at −0.9 V versus RHE. In addition, using STEM-EDS and operando XAFS, we have found that the oxides in the surface layer are surprisingly stable against reduction, with a significant amount of oxide species and dissolved oxygen remaining after 1 h of reaction at relatively high potentials (−0.91 V versus RHE). Furthermore, ethylene synthesis and methane suppression are due to the presence of these oxides. It is expected that the fundamental understanding extracted from our experimental study could aid the further design and optimization of oxide-derived Cu catalysts.